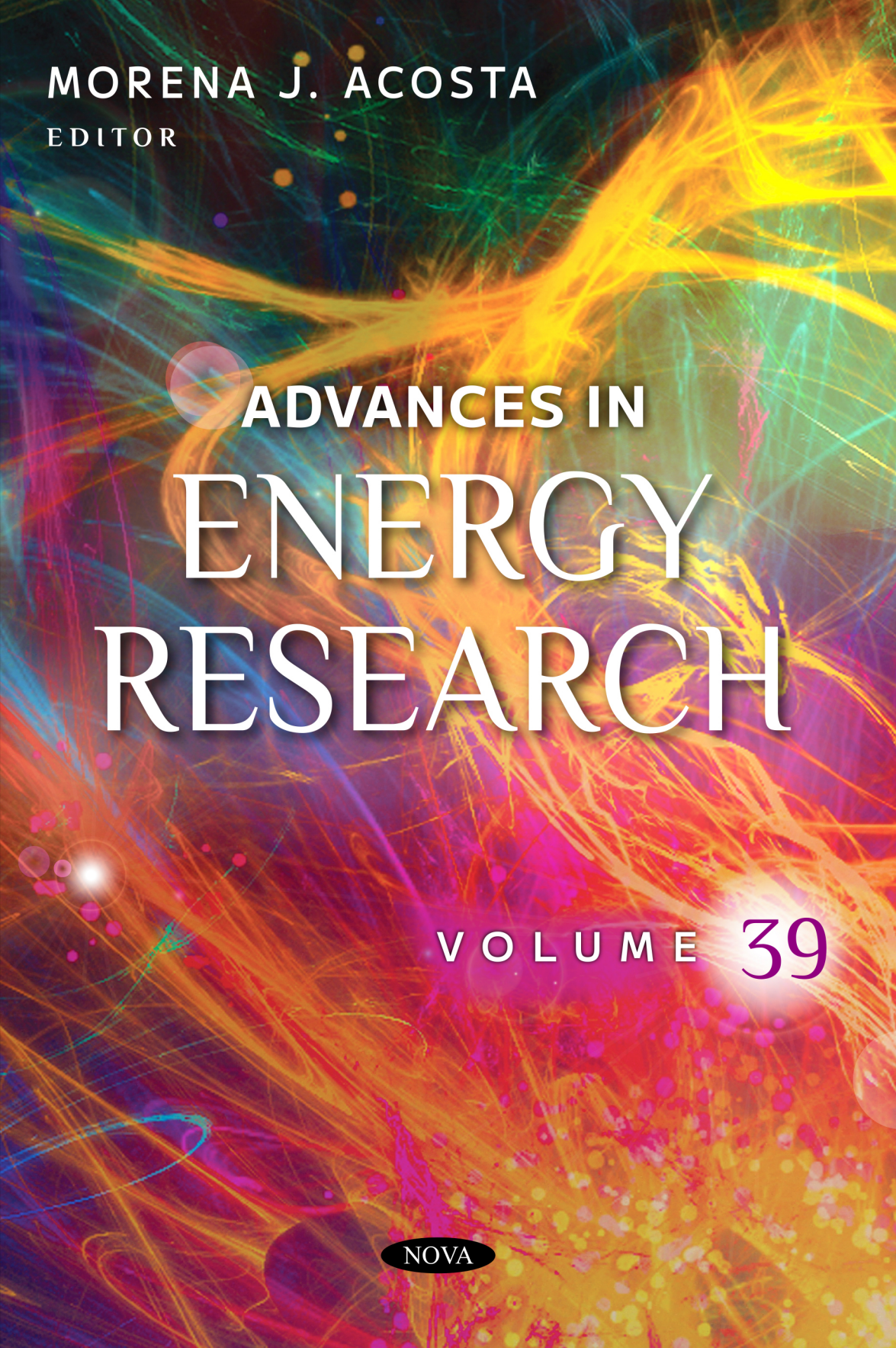
MORENA J. ACOSTA
EDITOR
ADVANCES IN
ENERGY
RESEARCH
VOLUME 39
NOVA

Advances in Energy Research

This is a numbered series focused on the latest research on energy.

Advances in Energy Research

Advances in Energy Research. Volume 38
Morena J. Acosta (Editor)
2023. ISBN: 979-8-88697-789-9 (Hardcover)
2023. ISBN: 979-8-88697-813-1 (eBook)

Advances in Energy Research. Volume 37
Morena J. Acosta (Editor)
2022. ISBN: 979-8-88697-392-1 (Hardcover)
2022. ISBN: 979-8-88697-407-2 (eBook)

Advances in Energy Research. Volume 36
Morena J. Acosta (Editor)
2022. ISBN: 978-1-68507-869-0 (Hardcover)
2022. ISBN: 978-1-68507-947-5 (eBook)

Advances in Energy Research. Volume 35
Morena J. Acosta (Editor)
2021. ISBN: 978-1-68507-373-2 (Hardcover)
2021. ISBN: N/A (eBook)

Advances in Energy Research. Volume 34
Morena J. Acosta (Editor)
2020. ISBN: 978-1-53618-980-3 (Hardcover)
2020. ISBN: 978-1-53618-997-1 (eBook)

Morena J. Acosta
Editor

Advances in Energy Research

Volume 39

nova
science publishers
www.novapublishers.com

Library of Congress Cataloging-in-Publication Data

ISBN: 979-8-88697-991-6 (eBook)

ISSN: 2157-1562

Published by Nova Science Publishers, Inc. † New York

Contents

Preface

This volume contains six chapters that detail recent advances in energy research. Chapter One addresses devices designed for both sunlight and artificial illumination as well as the emerging bifacial devices. Chapter Two describes the application of electrodeposited Ni-based, non-noble metal alloys and composites, as cathodes in the zero-gap membrane industrial cells. Chapter Three details the elaboration, characterization, modelling and application of the polyurethane/lead zirconate titanate composites for mechanical energy harvesting. Chapter Four discusses details of algal based biofuel production, factors affecting production, their efficient recovery and omics approach to improve the biofuel production. Chapter Five presents the use of floating offshore wind turbines for green electricity generation. Lastly, Chapter Six explains the findings of recent research on the generation of a hydrogen-based synthesis gas obtained from water electrolysis that uses an added carbon source.

Chapter 1

A Review of Different Dye-Sensitized Solar Cell Systems and Their Emerging Photovoltaic Applications

Carolina S. Hora[1,2]
Ana M. V. M. Pereira[1,2], PhD
M. Goreti. F. Sales[3], PhD
Dzmitry Ivanou[1,2], PhD
and Mendes[1,2,*], PhD

[1] LEPABE - Laboratory for Process Engineering, Environment, Biotechnology and Energy, Faculty of Engineering, University of Porto, Porto, Portugal
[2] ALiCE - Associate Laboratory in Chemical Engineering, Faculty of Engineering, University of Porto, Porto, Portugal
[3] BioMark@UC, Department of Chemical Engineering, Faculty of Sciences and Technology, University of Coimbra, Coimbra, Portugal

Abstract

After 30 years of research, dye-sensitized Solar Cells (DSSCs) became again a hot topic since their great performance for indoor applications was discovered. The simple fabrication, appealing aesthetics, adaptability for different performing requirements, and sustainability of the materials used are just a few key features that drive the research and development of this photovoltaic technology. Recently, DSSCs are emerging as efficient and easy to produce photovoltaic technology for

* Corresponding Author's Email: mendes@fe.up.pt.

In: Advances in Energy Research. Volume 39
Editor: Morena J. Acosta
ISBN: 979-8-88697-964-0

powering small electronic devices and wireless sensors within the Internet of Things (IoT) environment.

There is a myriad of reviews on specific components of a DSSC such as the sensitizer, counter-electrode, photoanode structure, among others. The present article aims at displaying an integrated view of the best performing devices based on redox couples, iodine, cobalt, and copper. This review addresses devices designed for both sunlight and artificial illumination as well as the emerging bifacial devices. Lastly, photovoltaic applications of the DSSCs will be reviewed, as well as the commercialization endeavors from various established companies.

Keywords: dye-sensitized solar cells, photovoltaic applications, artificial illumination

Introduction

Climate is changing and it is our responsibility to mitigate the consequences of global warming. A worldwide transition to renewable energy sources is needed to reduce the carbon-footprint. According to Figure 1 fossil fuels still represent over 60% of the world electricity consumption in 2020, while hydro, nuclear, wind and solar share 35.2% of the same market.

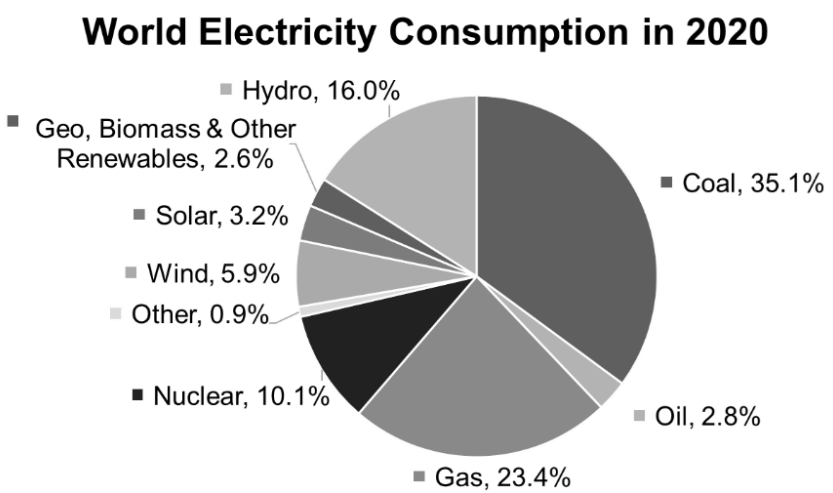

Figure 1. Energy sources for world electricity generation in 2020 (adapted from World Energy Data).

Solar radiation is by far the most powerful renewable energy source, delivering 23 000 TW per year while the world primary energy consumption was ca. 17.6 TW in 2020 (International Energy Agenct Solar Heating and Cooling Programme 2009; Statista). Thus, only 10% of the sun's power is needed to fulfill the world's energy requirements. The Renewables 2021 Global Status Report states that in 2020 it has been installed 256 GW of renewables power fields, where solar PV and wind power account for more than 90% of it (Ren2021 2021). In 2020, due to the SARS-CoV-2 pandemic and global lookdowns, electricity demand dropped abruptly, and favorable conditions for renewable power resulted in an increase of its market share, reaching ca. 29% of global electricity (Ren2021 2021). The rise in wind and solar electricity generation helped to decrease the share of fossil fuels, such as from coal, falling by a record of 4% (ca. -39.5 GW) (Ember 2021).

Currently, the solar PV market is still dominated by first- and second-generation solar cells. First-generation solar cells include single junction crystalline and polycrystalline silicon solar panels (c-Si and poly-Si) and represent ca. 85% - 90% of the market (Błaszczyk 2021). Second-generation cells introduced the heterojunction concept and use materials like cadmium telluride (CdTe), copper indium gallium selenide (CIGS), copper indium (di)selenide (CIS) and amorphous silicon (a-Si), that can be deposited as thin-films on glass or ceramic substrates (Andrade 2010); these solar cells only represent ca. 10% - 15% of the PV market (Błaszczyk 2021). Very recently, third-generation solar cells have started to enter the PV market because they offer simpler fabrication process, lower manufacturing costs, and better low-light performance (Mingsukang et al. 2017; S. Zhang et al. 2013; Kumar and Wong 2017; Kokkonen et al. 2021); this category includes dye-sensitized solar cells (DSSCs), perovskite solar cells (PSCs), organic solar cells (OSC), and quantum dot solar cells.

Since 1991, with the seminal work by Gräztel and O'Regan (O'Regan and Gratzel 1991), DSSCs have been rapidly evolving, reaching now efficiencies between 13% and 15% (AM1.5G) (Ren et al. 2022; Zeng, Tong, et al. 2020; Mathew et al. 2014; Ji et al. 2020; D. Zhang et al. 2021; NREL). Yet, they are routinely surpassed by PSCs (Jeong et al. 2020; Jung et al. 2019; Saliba et al. 2016; Jeon et al. 2018; Green et al. 2021), which in 2021 displayed a certified power conversion efficiency (PCE) of 25.7% (AM1.5G) (NREL). However, PSCs are an emerging technology with still major scientific and technological issues such as the use of lead in the most efficient perovskite absorbers (Grancini et al. 2017; Yang et al. 2016), and their high sensitivity to moisture and oxygen, leading to faster degradation of the perovskite absorber (Mesquita

et al. 2018). Among other third PV devices, DSSCs are the most mature technology, presenting interesting features as low toxicity, pleasant aesthetics, and, given the existent portfolio of different dyes, they are highly customizable (Mathew et al. 2014; Kakiage et al. 2015; Yella et al. 2011; Zhang et al. 2021). Additionally, the fabrication process of DSSCs is much simpler compared to other emerging PVs (Pallikkara and Ramakrishnan 2020; Sharma et al. 2018), and can be printed on both flexible, hard substrates or textiles (Kavan et al. 2017; Arbab et al. 2020; Yun et al. 2014).

Another advantage of DSSCs is the possibility of been illuminated from both sides, which helps achieve high photovoltage in diffuse light conditions (Freitag et al. 2017; Muñoz-García et al. 2021). In fact, outperforming other existing technologies, the high performance of DSSCs under dim or indoor lighting unveiled a paradigm shift in the field and introduced the potential of DSSCs to the indoor photovoltaic (IPV) market (Zhang et al. 2021; Freitag et al. 2017; Michaels et al. 2020; Tanaka et al. 2020). In these new testing conditions, DSSCs have already a record PCE of 34.5% (Zhang et al. 2021) and can truly rival other emerging PVs. At the moment, PSCs hold the highest PCE record of 40.2% (Dong et al. 2021) and OSCs display a record of 28.1% (Lee et al. 2018) under artificial illumination (1000 lx) (Figure 2a).

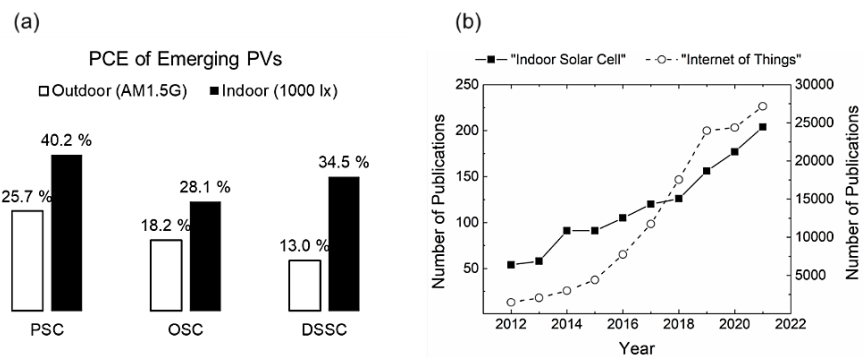

Figure 2. (*a*) Highest certified (Outdoor – AM1.5G, empty bars) (NREL) and highest reported (Indoor – 1000 lx, full bars) PCE of emerging PVs: perovskite solar cells (PSC) (Dong et al. 2021), organic solar cells (OSC) (Lee et al. 2018), and dye-sensitized solar cells (DSSC) (Zhang et al. 2021). (*b*) Number of publications released from 2012 to 2021 on the topic of "indoor solar cell" (full squares, on the left) and "Internet of Things" (open circles, on the right). Data source: Web of Science.

The Internet of Things (IoT) describes an ecosystem of smart objects equipped with sensors, all linked in network and working together to provide smart services to end users (Asghari et al. 2019). Since 2012, there has been an exponential growth in the number of publications regarding the topic "Internet of Things" (Figure 2b), and this has been translated into an increase in the IoT market, which is expected to reach 7.7 × 108 € in 2023 (Mathews et al. 2019). IoT related electronic devices, already present in our daily lives, are expected to surpass 75 billion units by 2025, and most of them are designed for indoor use (Michaels et al. 2020). Currently, these devices are powered by batteries that must be discarded when depleted. With the rampant increase of battery-powered devices, the number of batteries discarded is increasing exponentially, adding more environmental concern. Many IoT devices need little power to operate (Liu et al. 2018; Reddy et al. 2018), making DSSCs very attractive for powering these devices (Figure 2b).

The aesthetic appeal and the use of harmless chemicals, make DSSCs compatible for indoor applications. They can also be made much thinner and better suited to the indoor light spectrum than the conventional silicon PV cells; as DSSCs are the most suitable PV technology for indoor applications it is expected to become fully commercial quite soon (Rasheduzzaman et al. 2016; Freitag et al. 2017; Michaels et al. 2020; Tanaka et al. 2020; Aslam et al. 2020; Iqbal and Khan 2018; Venkateswararao et al. 2020; Cao et al. 2018; Mathews et al. 2019; Wu et al. 2017).

According to Figure 3, the DSSC market is primarily distributed among portable charging, building-integrated photovoltaics (BIPV)/building applied photovoltaics (BAPV), embedded electronics, outdoor advertising, and automotive-integrated photovoltaics (AIPV); the portable charging sector accounts for 33.3% of the total market share, followed by BIPV (24%) and embedded electronics (15%). This last sector is expected to grow in the coming years.

This chapter aims at reviewing the working principle of the most efficient devices, n-type DSSCs, and the role of the different redox mediators used under both simulated sunlight and artificial illumination. There are different ways to classify the DSSCs, either by the type of sensitizer – e.g., metal-based complexes vs. organic sensitizers, or by the type of counter-electrode, i.e., platinum counter-electrodes vs. polymer counter-electrodes. In this review, DSSCs are classified according to the redox couple used. Since there were published over 21,665 articles related to DSSCs, this review will only cover studies reporting power converting efficiencies over 9% for iodine, cobalt, and copper mediated devices. This review also highlights the systematic

development of DSSCs, presenting current and future photovoltaic applications of this technology.

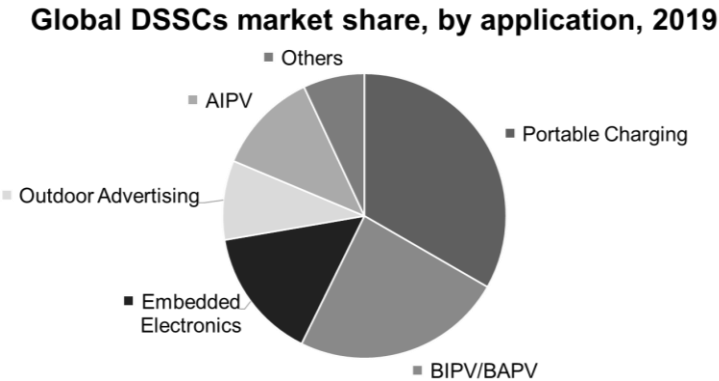

Figure 3. Global dye-sensitized solar cells market share, by application, in 2019 (adapted from Grand View Research).

Working Principle of Dye-Sensitized Solar Cells

A DSSC has three main elements: photoanode, counter-electrode and electrolyte. These third-generation solar cells mimic the natural process of photosynthesis, and the main difference from standard p-n junction devices is the separation between charge separation (light harvesting) and charge transport (Nogueira 2016). The operation of a DSSC starts by the photoexcitation of the dye molecules (1), where an electron moves from the highest occupied molecular orbital (HOMO) to the lowest unoccupied molecular orbital (LUMO) (Hagfeldt and Grätzel 2000). Thus, the sensitizer is responsible for the light harvesting.

In conventional DSSCs, the photoelectrode is n-type and then, after photoexcitation, the electrons from the valence band are injected into the conduction band of a semiconductor (2) and travel through the semiconductor mesoporous layer until the transparent conductive oxide (TCO) layer, which coats the glass substrate of the photoanode. Therefore, the semiconductor is responsible for the extraction and transport of the electrons.

From the photoelectrode, electrons travel through the external circuit until the counter-electrode, where they reduce the redox mediator (3). The redox

mediator diffuses until the mesoporous for regenerating the oxidized dye (4) (Heo et al. 2013; Grätzel 2004) (see Figure 4).

$$S + h\nu \rightarrow S^* \quad (1)$$

$$S^* \rightarrow S^+ + e^-_{CB} \quad (2)$$

$$Ox + e^-_{CE} \rightarrow Red \quad (3)$$

$$S^+ + Red \rightarrow Ox + S \quad (4)$$

$$S^* \rightarrow S \quad (5)$$

$$S^+ + e^-_{CB} \rightarrow S \quad (6)$$

$$Ox + e^-_{CB} \rightarrow Red \quad (7)$$

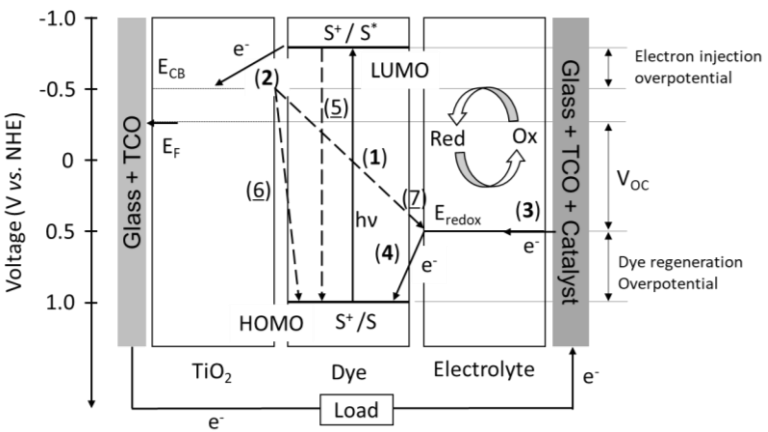

Figure 4. Schematic representation of DSSCs operating principle, kinetic reactions, and energy levels of materials used in DSSC. Forward reactions are represented by full arrows and recombination reactions are represented by dashed arrows. E_{CB} – conduction band energy; E_F – Fermi energy; S – sensitizer in the ground state; S^+ – sensitizer in the oxidized state; S* – excited state of the sensitizer; e^- – electrons; E_{redox} – electrolyte redox potential; TCO – transparent conductive oxide; LUMO – lowest unoccupied molecular orbital; HOMO – highest occupied molecular orbital.

There are competing reactions in which electrons flow through different pathways, namely, decay from the excited state to the ground state at the dye molecules (5), injected electrons may recombine with oxidized dye molecules

(6), and injected electrons may recombine with the oxidized redox mediator at the mesoporous layer (7) (Andrade et al. 2010).

Reactions 1 and 2 are considered irreversible because their forward kinetic constants are much higher than for the corresponding reverse reactions (5 and 6, respectively). Thus, the reaction between the photoinjected electrons with the oxidized species of the redox shuttle (7) is the preferential recombination mechanism, and the main source of the dark current (Maçaira et al. 2014).

To minimize the recombination at the TCO layer, a very thin layer of TiO_2 (known as blocking layer) is often deposited on the TCO layer for mitigating recombination between injected electrons and the reduced redox species (Góes et al. 2012; Kim et al. 2013; Hora et al. 2019; Eom et al. 2014). The overall recombination rate of the injected electrons with the reduced redox mediator depends on several factors such as, photoelectrode mesoporous layer thickness, chemical composition of the sensitizer, redox mediator diffusion rate, co-adsorbant properties of the reduced redox species. (Hamann et al. 2008).

The energy performance of a solar cell is first characterized by the power conversion efficiency (PCE), which depends on the incident light intensity (I_S), photocurrent density at the maximum power point (J_{MPP}), and open-circuit photopotential at the maximum power point (V_{MPP}). Those parameters can be obtained from the *J-V* characteristic curve (Figure 5).

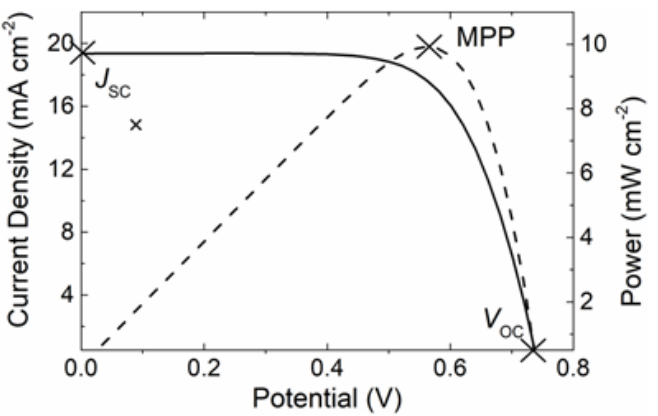

Figure 5. Typical *J-V* curve and power plot of a solar cell; J_{SC} – short circuit current density, MPP – maximum power point; V_{OC} – open circuit potential.

At 0 V, the device is at short-circuit where the highest current density is produced, J_{SC}; at 0 mA, when there is no current flow, the circuit is open and

the potential generated is the V_{OC}. The power plot is calculated multiplying the current density by the potential, defining the point where the device reaches its maximum power output (or maximum power point, MPP). The fill factor, η_{FF}, is the ratio between the power delivered at the maximum power point and the power obtained from the product of J_{SC} by V_{OC}, as indicated in Eq. 1and the power conversion efficiency is obtained from the product between J_{SC} and V_{OC}, corrected by η_{FF} and normalized by the irradiance, as indicated in Eq. 2:

$$\eta_{FF} = \frac{P_{MPP}}{J_{SC}V_{OC}} = \frac{J_{MPP}V_{MPP}}{J_{SC}V_{OC}} \quad (1)$$

$$\eta_{PCE} = \frac{J_{SC}V_{OC}}{I_S}\,\eta_{FF} \times 100 \quad (2)$$

Since the PCE efficiency is related to the product of $J_{SC} \times V_{OC}$, optimizing the PCE is a trade-off between increasing the current density, which often implies decreasing the delivering potential, and the delivering potential (Salim et al. 2014; Hagfeldt et al. 2010; Koops et al. 2009; Kinoshita et al. 2015; Ozawa et al. 2016; Krishna et al. 2017). The maximum value of V_{OC} generated under illumination corresponds to the difference between the Fermi energy (E_F) of the semiconductor and the electrolyte redox potential (E_{redox}), Figure 4.

To ensure maximum V_{OC}, it is crucial to mitigate the dark current. Dark current, or recombination, is mostly related to the capture of injected electrons by the oxidized species of the redox mediator. Lower electron recombination rates lead to longer electron lifetimes, lower dark current, and improved η_{FF} (Sugathan et al. 2015). The J_{SC} is intrinsically associated with the ability of the sensitizer to absorb the photons with energy above the sensitizer band gap and injecting them in the conduction band of the photoanode. To characterize a sensitizer, a typical strategy is then to measure the incident photon to current conversion efficiency (IPCE), as function of the incident photon wavelength, which is defined as the ratio of the number of electrons flowing through the external circuit ($N_{electrons}$) and the number of incident photons with a given wavelength λ ($N_{photons}$), as indicated in Eq. 3:

$$\mathrm{IPCE}(\lambda) = \frac{N_{electrons}}{N_{photons}} = \frac{\frac{q\,N_{electrons}}{t}}{\frac{q\,N_{photons}}{t}}, if\ I_{SC} = \frac{q\,N_{electrons}}{t}, \text{then } \mathrm{IPCE}(\lambda) = \frac{I_{SC}}{\frac{q\,N_{photons}}{t}} \quad (3)$$

where q is the elementary charge, t is the time and I_{SC} is the photocurrent at short-circuit. The power of incident light (P_{in}) is related to $N_{photons}$, and it is given by Eq. 4:

$$P_{\text{in}} = \frac{N_{\text{photons}}}{t} h\,\nu = \frac{N_{\text{photons}}}{t} h \frac{c_0}{\lambda} \Leftrightarrow N_{\text{photons}} = \frac{t\,\lambda\,P_{in}}{c_0\,h} \quad (4)$$

where h is the Planck constant, ν is the frequency, c_0 is the speed of light and λ is the wavelength. Introducing Eq. 4 in Eq. 3, the IPCE equation can be written as (Andrade 2010):

$$\text{IPCE}\,(\lambda) = \frac{I_{\text{SC}}}{q\frac{t\,\lambda\,P_{\text{in}}}{c_0\,h}} = \frac{I_{\text{SC}}\,h\,c_0}{q\,\lambda\,P_{\text{in}}} = \frac{I_{\text{SC}}\,(\lambda)}{P_{\text{in}}\,(\lambda)} \frac{1240}{\lambda} \times 100\% \quad (5)$$

As Eq. 5 shows, the IPCE measures the spectral response under short-circuit conditions. There are two methods for obtaining the IPCE: AC mode and DC mode. The most common is the DC mode in which the photocurrent is measured under a monochromatic light source with a fixed photon flux (Yang et al. 2013). The IPCE can be used to estimate the total photocurrent from the integral of the product between the incident photon flux density (I_{photon}) and the IPCE for a range of wavelengths, as indicated in Eq. 6 (Yang et al. 2013):

$$J_{\text{SC}} = \int_{\lambda_{\text{min}}}^{\lambda_{\text{max}}} I_{\text{photon}}(\lambda) \cdot \text{IPCE}\,(\lambda)\,d\lambda \quad (6)$$

The IPCE of a device depends mainly on three factors: light-harvesting efficiency of the dye (LHE), efficiency of electron injection (Φ_{INJ}), and collection efficiency of the injected electrons at the TCO (Φ_{COLL}):

$$\text{IPCE}\,(\lambda) = \text{LHE}\,(\lambda)\,\Phi_{\text{INJ}}\,(\lambda)\,\Phi_{\text{COLL}}(\lambda) \quad (7)$$

LHE depends on the adsorption surface area of the mesoporous layer and on the molar extinction coefficient of the sensitizer. The first is optimized to display the largest specific surface area without compromising the redox mediator diffusion while the second depends chiefly on chemical nature of the sensitizer. Anyway, for increasing the LHE a light-scattering layer, composed of larger TiO_2 particles and applied over the mesoporous layer, is used to reflect back part of the crossing radiation without imposing a significant

transport resistance on the redox mediator (Sommeling et al. 2006; Usami 1997; Kuang et al. 2006; Nazeeruddin et al. 1993). The electron injection efficiency, Φ_{COLL}, depends on the residence time of the reduced redox species at the mesoporous and light-scattering layers and on the current density (Sommeling et al. 2006). The collection efficiency of the injected electrons, Φ_{INJ}, depends on the ratio of photons harvested by the sensitizer that are successfully injected into the conduction band of the semiconductor; this process competes with the quenching of the excited sensitizer. The charge injection in a good performing solar cell should be at least 100 times faster than the decay rate constant of the dye (Grätzel 2005; Hagfeldt et al. 2010).

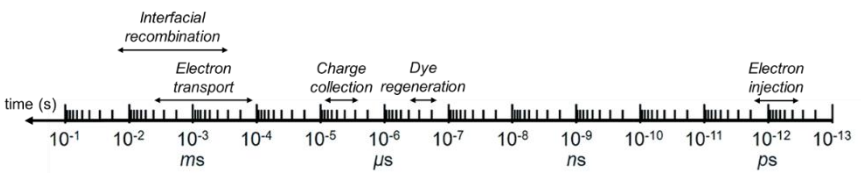

Figure 6. Dynamic competition of electrochemical processes during operation of a DSSC (adapted from Ji et al. 2018).

Besides the steady-state *J*-*V* curve and IPCE spectra, dynamic techniques such as electrochemical impedance spectroscopy (EIS) allow the identification of charge transfer kinetics, which occur on different time scales as shown in Figure 6 (Ji et al. 2018). To measure the impedance spectra, a small sinusoidal potential perturbation is normally applied, and the current response recorded as a function of the applied frequency (Brett and Brett 1993). The frequency-potential perturbation is typically performed under open-circuit conditions with a modulation signal of magnitude V_0:

$$V(t) = V_{OC} + V_0 \cos(\omega t) \tag{8}$$

The corresponding response has a period equal to the period of the potential perturbation, but it is phase shifted by φ:

$$I(t) = I_{OC} + I_0 \cos(\omega t - \varphi) \tag{9}$$

where V_0 and I_0 are, respectively, the amplitudes of potential and current signals, ω is the radial frequency and I_{OC} (open-circuit current) is zero (Andrade 2010).

The impedance, Z, is the ratio between potential and current:

$$Z = \frac{V_0 \cos(\omega t)}{I_0 \cos(\omega t - \varphi)} = Z_0 \frac{\cos(\omega t)}{\cos(\omega t - \varphi)} \tag{10}$$

Applying complex notation to this equation we obtain (Barsoukov and Macdonald 2005):

$$Z = Z_0 \frac{e^{j\omega t}}{e^{(j\omega t - j\varphi)}} = Z_0 e^{j\varphi} = Z_0 (\cos\varphi + j \sin\varphi) \tag{11}$$

$$Z' = Z_0 \cos\varphi \tag{12}$$

$$Z'' = Z_0 \sin\varphi \tag{13}$$

where j is the imaginary number and Z' is the real component of the impedance and Z'' the imaginary component (Eq. 13). Figure 7a shows a typical Nyquist plot of a DSSC, which sweeps a defined frequency range to examine the different electrochemical processes that occur in the solar cell at different times (Figure 1.6).

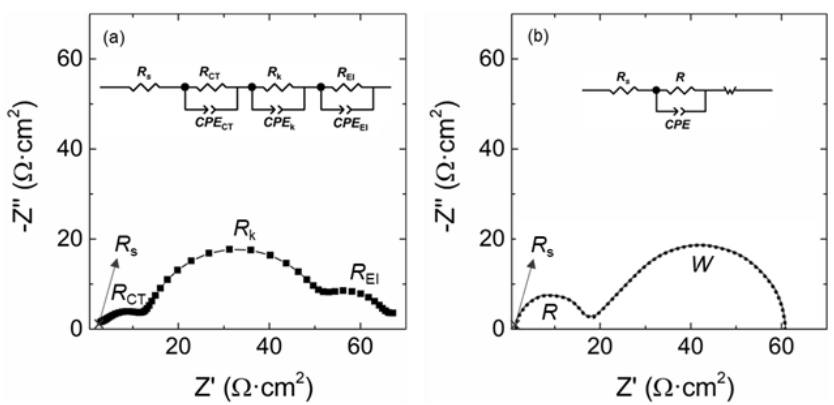

Figure 7. (*a*) Typical Nyquist plot of a DSSC and equivalent circuit used to fit the electrochemical impedance spectra; R_s – series resistance; R_{CT} – charge-transfer resistance; R_k – charge-recombination resistance; R_{EI} –diffusion resistance in the electrolyte; CPE_{CT} – charge-transfer constant phase element; CPE_k – charge-recombination constant phase element; CPE_{EI} – diffusion constant phase element. (*b*) Nyquist plot and equivalent circuit representing a Nernst-Planck diffusion, W – Warburg diffusion.

Analyzing Figure 7a from high to low frequencies (from left to right in the figure), semicircle #1 is assigned to the redox reaction at the counter-electrode; semicircle #2 is related to electron transfer in the TiO_2/electrolyte interface; and semicircle #3 is ascribed to the Nernst diffusion of the redox couple (Wang et al. 2005; Choi and Kim 2018; Andrade et al. 2010).

EIS is a powerful diagnostic tool that can be used to quantify the electron transport, charge accumulation, and recombination as well as electrolyte diffusion by fitting the impedance spectra obtained to an equivalent circuit model (Fabregat-Santiago et al. 2005). Figure 7a shows the most used equivalent circuit to study the electronic and ionic transport in DSSCs. The first element of the EIS is a resistor, representing the series resistance of the device (R_s). Next, assembled in parallel, are another resistor with a capacitor; in this case, the resistor represents the kinetics of the electrochemical reaction and the capacitor embodies the charge separation in the counter-electrode/electrolyte interface (Andrade et al. 2010).

The resistor is defined as the charge-transfer resistance between counter-electrode and electrolyte (R_{CT}) and as the capacitor is rarely ideal, the double layer capacitor is represented by a constant phase element (CPE_{CT}). Next, the equivalent circuit shows a third resistor and a second capacitor connected in parallel, representing the charge-recombination resistance in the photoanode/electrolyte interface (R_k and CPE_k). Lastly, the equivalent circuit shows another resistor and a constant phase element connected in parallel, representing the diffusion resistance in the electrolyte (R_{EI} and CPE_{EI}). If the electrolyte permeates through a porous media, the diffusion will be represented by the Nernst-Planck element, or Warburg diffusion for a finite length (Quang et al. 2018), as shown on Figure 7b.

Dye-Sensitized Solar Cells Systems

This review article aims at presenting an overview of the most typical and efficient DSSCs that can be used to synergistically power electronic devices, highlighting the advantages and disadvantages of each DSSC configuration.

There are some guidelines that must be met when assembling high performing DSSCs, with each component of the device incorporating fundamental requirements. The most common semiconductor used for electron transport in DSSCs is TiO_2 – anatase. Titania has a wide band gap (*ca.* 3.2 V), a good conduction band alignment with the LUMO level of most dyes, and only absorbs light in the UV range. Moreover, it provides decent

electronic conductivity, low back-electron recombination with electrolyte, and has high chemical stability and low toxicity (Pallikkara and Ramakrishnan 2020; Gnida et al. 2021).

The porosity and morphology of the semiconductor determines the amount of dye adsorbed on its surface and, consequently, how well it captures the incident light. So, the photoelectrode of a DSSC must have a large specific area, and this can be accomplished by applying a mesoporous layer. This layer, which is a semi-transparent film composed of highly dispersed anatase nanoparticles (with an average size ranging 20-30 nm), ensures very high surface area for dye adsorption – for a 10 µm mesoporous layer the specific surface area is *ca*. 120 m^2/m^2. The mesoporous layer is often combined with a light-scattering layer, composed of larger nanoparticles (*ca.* 400 nm) of TiO_2 – anatase, which increase the optical path of light and enhance absorption in thinner films (Usami 1997; Gnida et al. 2021).

A TiO_2 blocking layer, also known as electron extraction layer, is also common practice to prevent direct contact between the TCO substrate and the redox couple, thus minimizing the recombination at the photoanode (Góes et al. 2012; Kim et al. 2013; Hora et al. 2019; Eom et al. 2014; Cameron and Peter 2003). Lastly, a chemical bath deposition of $TiCl_4$, which after the sintering process originates TiO_2, is often applied to lower the recombination rate constant between conduction band electrons (e^-_{CB}) and the redox shuttle, improving the quantum efficiency of electron injection between the sensitizer and the titania layer and, consequently, increases the photocurrent. Moreover, it increases electron lifetime, which leads to higher electron diffusion length (Hora et al. 2019; Sommeling et al. 2006; O'Regan et al. 2007). This post-treatment also enhances improves the crystallinity of the TiO_2 layer, and the larger surface area leads to better dye adsorption (Lee et al. 2012).

The performance of DSSCs is restricted by the Shockley-Queisser limit (33%) (Shockley and Queisser 1961), which implies that the sensitizer should absorb all sunlight photons with energy above 1.3-1.4 eV (corresponding to a wavelength range of 940-890 nm) (Peter 2011). Ideally, the LUMO level of the sensitizer should match the edge of the conduction band of the TiO_2 to guarantee fast electron injection and minimize the electron injection overpotential (Figure 4). The HOMO level of the dye must be sufficiently low to accept electrons from the redox mediator to allow efficient regeneration of the dye (Gong et al. 2012). Anchoring groups, such as –COOH, $–SO_3H$, $–H_2PO_3$, are essential for strong bonds between the TiO_2 and the sensitizer. They also enhance the electron injection into the semiconductor conduction band (Hagfeldt et al. 2010).

Aggregation of dye molecules on the semiconductor surface must be avoided, either by using co-adsorbents (cholic acid (Horiuchi et al. 2004) or chenodeoxycholic acid (Ito et al. 2006)) or anchoring groups (carboxylic acid (Nazeeruddin et al. 1993), alkoxy-silyl (Matta et al. 2014) or phosphoric acid (Kryman et al. 2016)), to avoid competition between electron injection as well as recombination between e^-_{CB} and the redox shuttle. The chosen sensitizer must have long stability by enduring at least 10^8 redox turnovers, which corresponds to approximately 20 years of operation; it should also have low toxicity and high solubility (Nazeeruddin et al. 1993; Goncalves et al. 2008).

The choice of redox mediator has a tremendous effect on the performance of the solar cell, and significant research has been conducted for developing new and stable redox couples. While cobalt and copper electrolytes lead the record for the highest performing DSSCs, iodine solar cells remain ubiquitous as Figure 8 shows.

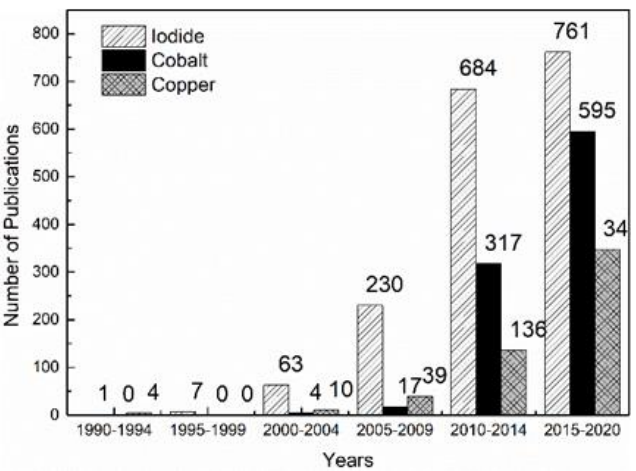

Figure 8. Number of publications released per year from a simple literature search using keywords "dye sensitized solar cells" and (*orange*) "iodide," "I3"; (*green*) "cobalt," "Co(III)"; (*red*) "copper," "Cu(II)." Data source: Web of Science.

Iodine-Mediated Solar Cells

Iodine electrolytes are still the most researched redox couple used in DSSCs, and one of their major advantages is ascribed to its slow recombination with TiO_2 e^-_{CB}. This reduces the main recombination pathway in DSSCs, and

therefore the cathodic dark current, while establishing a practically quantitative collection of photogenerated charge carriers (Yella et al. 2017; Feldt et al. 2011). The small size of the iodine redox couple helps to achieve fast diffusion through the mesopores of the titania layer and increases the photocurrent for a given electrolyte concentration (Hardin et al. 2012).

Introducing a dense TiO_2 blocking layer between the FTO and the semiconductor can effectively prevent short-circuits when the electrolyte encounters the conductive glass after permeating through the mesopores of the titania layer. Usually, iodine electrolytes are used with ruthenium sensitizers, and the mismatch between the redox potential of the I^-/I_3^- and the HOMO level increases the overpotential of the dye regeneration, decreasing the open-circuit potential of the solar cells (Yella et al. 2017; Yella et al. 2011; Kavan et al. 2011).

The dye regeneration step is also complicated due to the two-electron reduction reaction of I^- to I_3^- (Boschloo and Hagfeldt 2009). The I^-/I_3^- redox mediator absorbs a significant part of the visible light spectrum (Nusbaumer et al. 2003) and is corrosive towards most metals. This greatly limits the choice of counter-electrode materials and prevents the use of metal current collectors, namely silver, when scaling up the DSSCs (Son et al. 2018; Boschloo and Hagfeldt 2009).

Ruthenium dyes became very popular among sensitizers after the breakthrough work by Gräztel and O'Regan (O'Regan and Gratzel 1991), who revolutionized the field by replacing a compact film of TiO_2 by a mesoporous layer, increasing the internal surface area and significantly enhancing the dye adsorption. The incident light was harvested by a trinuclear ruthenium complex and a PCE of 7.9% was achieved. Ruthenium sensitizers consist of a central Ru ion with ancillary ligands and anchoring groups. Therefore, when the sensitizer absorbs photons, an electron from the metal d-orbital jumps to the ligand π^* orbital, and thus metal-to-ligand charge transfer (MLCT) is responsible for the light absorption in the visible range of the spectrum (Goncalves et al. 2008). Overall, the HOMO level is attributed to the Ru and electron donating ligands, whereas the LUMO level is localized on the polypyridyl ligand. This distribution enhances the injection of electrons into the semiconductor conduction band through chemical bonding and regeneration of the oxidized state of the sensitizer (Zhang et al. 2013).

In 1993, Nazeeruddin et al. (Nazeeruddin et al. 1993) introduced another Ru sensitizer, the N3 complex (Figure 9a), which presents a broad absorption in the visible range of the spectrum, long lifetime of the excited state, its LUMO nearly matches the conduction band of the TiO_2, and it displays a high

thermal stability. Devices with N3 dye display a PCE over 10% under 1-sun (Nazeeruddin et al. 1993; Grätzel 2003) (Table 1). The N749 (Figure 9b), also known as "black dye," has three thiocyanate anionic ligands that stabilize the excited states by electron donation to Ru, leading to a red-shift of the MLTC bands et al. 1997). This dye allows efficient sensitization over the whole visible spectrum, even extending to the near-infrared region (*ca.* 920 nm), originating in devices with PCE of 10.4% (Nazeeruddin et al. 2001), further improved to 11.1% (Chiba et al. 2006) (Table 1). N719 (Figure 9c) was also developed from the N3 complex by deprotonation of the carboxylic acid groups, lowering the HOMO-LUMO gap of the dye and resulting in an absorption onset around 1.65 eV (750 nm), which is far from the optimum 1.3-1.4 eV (Peter 2011; Nazeeruddin et al. 1999).

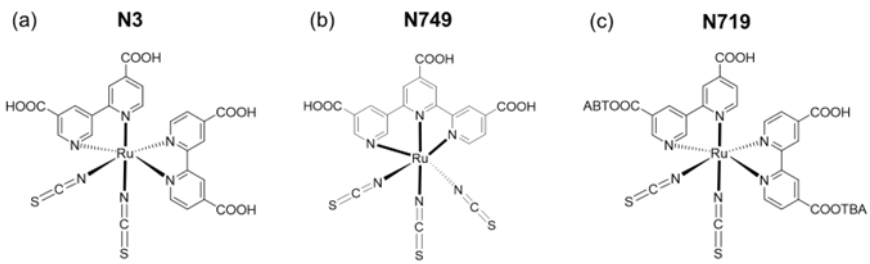

Figure 9. Chemical structure of most common and efficient Ru-complexes: (*a*) N3, (*b*) N749, and (*c*) N719.

Other successful ruthenium dyes were developed (Nazeeruddin et al. 2005; Ito et al. 2008; Hussain et al. 2014; Hu et al. 2014), but only a few surpass the 10% threshold. Chang et al. reported a PCE of 10.05% (Chang and Chi 2017); Ozawa et al. achieved a PCE of 11.1% with TUS-38 dye bearing a *n*-hexylthiophene modified terpyridine derivative ligand and enhanced the PCE of the device to 11.9% by replacing the 1,2-dimethyl-3-*n*-propylimidazolium iodide (DMPII) by 1-ethyl-3-methylimidazolium iodide (EMII) in the electrolyte solution (Ozawa et al. 2016). A remarkable PCE of 12.0%, certified by the National Measurement Laboratory in Taiwan, was achieved by Chiang et al. employing a $Pt_{49}Co_{23}Fe_{28}$ nanowire as counter-electrode and sensitizing the photoanode with a Ru-based dye, PRT-22 (Chiang et al. 2018) (Table 1). The PtCoFe nanowire in combination with the PRT-22 increases the photocurrent and decreases the R_{CT}, a direct result of the exceptional catalytic activity towards the I_3^- reduction. Chiang et al. surpassed the 12% threshold with their champion DSSC, at 12.29% of PCE, and became the best performing Ru-based device (Table 1).

Table 1. Photovoltaic characteristics of iodine-based DSSCs with PCE > 9% under solar simulated sunlight (AM1.5 G)

Dye	CE	Electrolyte	V_{OC} (mV)	J_{SC} (mA·cm^{-2})	η_{FF}	η_{PCE} (%)	Year	Ref.
N3	Pt	I_2, LiI, tBP	720	18.2	0.73	10.0	1993	(Nazeeruddin et al. 1993)
N749	Pt	I_2, LiI, DMPII, tBP	720	20.5	0.70	10.4	2001	(Nazeeruddin et al. 2001)
N719	Pt	I_2, LiI, MBII, tBP	750	17.0	0.72	9.18	2003	(Nazeeruddin et al. 2003)
N719	Pt	I_2, LiI, GuSCN	796	17.8	0.75	10.6	2003	(Grätzel 2003)*
N719	Pt	I_2, LiI, DMPII, tBP	764	18.2	0.74	10.2	2004	(Wang et al. 2004)
N621	Pt	A6141 w/GuSCN	777	16.8	0.73	9.57	2005	(Nazeeruddin et al. 2005)
N719	Pt	A6141 w/GuSCN	846	17.7	0.75	11.2	2005	(Nazeeruddin et al. 2005)
N749	Pt	I_2, LiI, DMPII, tBP	736	20.9	0.72	11.1	2006	(Chiba et al. 2006)*
D205	Pt	I_2, LiI, BMII, GuSCN, tBP	710	18.7	0.71	9.40	2008	(Ito et al. 2008)
N719	Pt	I_2, LiI, BMII, GuSCN, tBP	789	18.2	0.70	10.1	2008	(Ito et al. 2008)
CYC-B11	Pt	I_2, LiI, DMII, GuSCN, tBP	743	20.1	0.77	11.5	2009	(Chen et al. 2009)
YD-2	Pt	I_2, LiI, DMII, GuSCN, tBP	770	18.6	0.76	11.0	2010	(Bessho et al. 2010)
YDD6+ CD4+ YD2-*o*-C8	Pt	I_2, LiI, PMII, tBP	753	18.0	0.72	10.4	2012	(Wu et al. 2012)
N749	Pt	I_2, LiI, DMPII, tBP	727	20.4	0.72	10.8	2012	(Ozawa et al. 2012)
N749	Pt	I_2, LiI, DMPII, tBP	727	20.5	0.72	10.7	2012	(Han et al. 2012)
N749+Y1	Pt	I_2, LiI, DMPII, tBP	743	21.3	0.72	11.4	2012	(Han et al. 2012)*
N719 (w/DCA)	Pt	I_2, LiI, DMPII, tBP	749	16.9	0.74	9.32	2014	(Hussain et al. 2014)
MH13 (w/DCA)	Pt	I_2, LiI, DMPII, tBP	660	20.6	0.72	9.71	2014	(Hussain et al. 2014)
N719	Pt	TEAI, TMAI, TBAI, NaI, KI, LiI, I_2, tBP	779	18.0	0.70	9.86	2014	(Hu et al. 2014)

Dye	CE	Electrolyte	V_{OC} (mV)	J_{SC} (mA·cm^{-2})	η_{FF}	η_{PCE} (%)	Year	Ref.
TFRS-52	Pt	I_2, LiI, DMPII, tBP	850	15.2	0.76	9.90	2014	(Hu et al. 2014)
LD31	Pt	I_2, LiI, PMII, tBP	699	20.0	0.71	9.95	2014	(Wang et al. 2014)
LD31+AN-4	Pt	I_2, LiI, PMII, tBP	704	20.3	0.72	10.3	2014	(Wang et al. 2014)
XW1+C1	Pt	I_2, LiI, PMII, tBP	746	17.5	0.71	9.24	2014	(Wang et al. 2014)
N719	Pt	I_2, LiI, PMII, tBP	806	17.7	0.68	9.63	2014	(Wang et al. 2014)
XW4+C1	Pt	I_2, LiI, PMII, tBP	736	20.2	0.71	10.5	2014	(Wang et al. 2014)
N749+ U01	Pt	I_2, LiI, DMPII, tBP	722	20.4	0.72	10.6	2014	(Islam et al. 2014)
N749	NDG/CoS	I_2, LiI, DMPII, tBP	710	20.4	0.74	10.7	2014	(Bi et al. 2014)
DX3	Pt	I_2, LiI, DMPII, tBP	556	30.3	60.5	10.2	2015	(Kinoshita et al. 2015)
LD14+ LDD1	Pt	I_2, LiI, PMII, tBP	705	21.3	0.69	10.4	2015	(Shiu et al. 2015)
XW17	Pt	I_2, LiI, PMII, tBP	700	18.8	0.72	9.5	2015	(Tang et al. 2015)
XW16+WS-5	Pt	I_2, LiI, PMII, tBP	773	19.0	0.72	10.4	2015	(Tang et al. 2015)
XW17+WS-5	Pt	I_2, LiI, PMII, tBP	748	20.3	0.72	10.9	2015	(Tang et al. 2015)
ADEKA-1+ LEG4	Pt	I_2, LiI, NaI, DMPII, EMII, TBAI, THAI, tBP, MP, GuSCN	783	19.1	0.75	11.2	2015	(Kakiage et al. 2015)
XW11+ C1	Pt	I_2, LiI, PMII, tBP	746	19.5	0.74	10.6	2015	(Xie et al. 2015)
XW10+WS-5	Pt	I_2, LiI, PMII, tBP	765	19.0	0.76	11.0	2015	(Xie et al. 2015)
XW11+WS-5	Pt	I_2, LiI, PMII, tBP	760	20.3	0.74	11.5	2015	(Xie et al. 2015)
YD23	Pt	I_2, LiI, PMII, tBP	740	17.1	0.71	9.00	2016	(Chou et al. 2016)
YD24	Pt	I_2, LiI, PMII, tBP	730	17.3	0.72	9.19	2016	(Chou et al. 2016)
Y1A1	PVP-Pt	I_2, LiI, PMII, tBP	658	18.6	0.75	9.22	2016	(Liu et al. 2016)
C101		I_2, LiI, BMII, tBP, GuSCN	734	19.3	0.72	10.2	2016	(Lou et al. 2016)
TUS-38	Pt	I_2, LiI, EMII, tBP	702	23.4	0.72	11.9	2016	(Ozawa et al. 2016)
N719	Pt	I^-/I_3^-	700	22.6	0.66	11.4	2016	(Park et al. 2016)
RK-3	Pt	I_2, LiI, DPMII, tBP, GuSCN	750	16.4	0.75	9.30	2017	(Park et al. 2017)

Table 1. (Continued)

Dye	CE	Electrolyte	V_{OC} (mV)	J_{SC} (mA·cm^{-2})	η_{FF}	η_{PCE} (%)	Year	Ref.
N719	Co-Fe-Se	I_2, LiI, DPMII, tBP	762	18.4	0.69	9.58	2017	(Jiang et al. 2017)
WS-69	Pt	I_2, LiI, DPMII, tBP	696	19.4	0.67	9.03	2017	(Zhang et al. 2017)
WS-5+ WS-69	Pt	I_2, LiI, DPMII, tBP	753	19.6	0.68	10.1	2017	(Zhang et al. 2017)
XW11	Pt	I_2, LiI, PMII, tBP	727	18.3	0.70	9.30	2017	(Yang et al. 2017)
XW28	Pt	I_2, LiI, PMII, tBP	715	19.4	0.73	10.1	2017	(Yang et al. 2017)
TF-*t*Bu_C_3F_7	PVP-Pt	I_2, LiI, DPMII, tBP	767	18.5	0.71	10.1	2017	(Chang and Chi 2017)
N719	$CoSe_2$-1.1	I_2, NaI, TBAI, tBP	809	17.7	0.71	10.2	2017	(Jia et al. 2017)
LG6	Pt	I_2, LiI, DPMII, tBP	690	19.6	0.71	9.64	2017	(Krishna et al. 2017)
LG5	Pt	I_2, LiI, DPMII, tBP	680	21.0	0.71	10.2	2017	(Krishna et al. 2017)
FW-1+ WS-5	Pt	I_2, LiI, PMII, tBP	761	18.9	0.71	10.2	2017	(Xiang et al. 2017)
MD7	Pt	I_2, LiI, DPMII, tBP	753	17.7	0.68	9.03	2018	(Desta et al. 2018)
N719+ RK-1	Pt	Iodolyte	733	25.1	0.51	9.45	2018	(Mehmood et al. 2018)
N719	Co-Fe-MoS_x-2	I_2, LiI, PMII, tBP	838	18.1	0.64	9.63	2018	(Xu et al. 2018)
C268+ SC-4	Pt	I_2, DMII, EMII, Sulfolane, NBB, GuSCN	779	18.1	0.71	10.0	2018	(Wang et al. 2018)
IQ-4	Pt	I_2, LiI, DPMII, tBP,	740	17.5	0.71	9.24	2018	(Jiang et al. 2018)
WS-84	Pt	I_2, LiI, DPMII, tBP,	759	19.0	0.70	10.1	2018	(Jiang et al. 2018)
JY53	Pt	I_2, LiI, DPMII, tBP, GuSCN	814	18.9	0.61	9.42	2018	(Han et al. 2018)
JY55	Pt	I_2, LiI, DPMII, tBP, GuSCN	829	19.2	0.63	10.1	2018	(Han et al. 2018)
N719	Pt	I_2, LiI, DPMII, tBP	700	24.9	0.64	11.3	2018	(Thogiti et al. 2018)
N719	Pt	I_2, LiI, BMII, tBP	710	23.4	0.67	11.7	2018	(Dhonde et al. 2018)
PRT-22	$Pt_{49}Co_{23}Fe_{28}$ nanowire	I_2, LiI, DPMII, tBP, GuSCN	741	23.9	0.68	12.0	2018	(Chiang et al. 2018)*

Dye	CE	Electrolyte	V_{OC} (mV)	J_{SC} (mA·cm^{-2})	η_{FF}	η_{PCE} (%)	Year	Ref.
N719	Co-N-CNFs	I_2, LiI, PMII, tBP, GuSCN	742	18.0	0.68	9.05	2019	(Li et al. 2019)
N719	CoS NSAs	I_2, LiI, DPMII, tBP	753	16.9	0.74	9.46	2019	(Feng et al. 2019)
N719	Co–Cu–WS_x	I_2, LiI, DPMII, tBP	798	17.7	0.68	9.61	2019	(Qian et al. 2019)
N719	Pt	I_2, LiI, DPMII, tBP	739	17.0	0.77	9.62	2019	(Kim et al. 2019)
N719	Te-SMC	I_2, LiI, DPMII, tBP	733	17.1	0.77	9.67	2019	(Kim et al. 2019)
N719	Cu-Ni-$CoSe_x$	I_2, LiI, DPMII, tBP	783	17.9	0.69	9.71	2019	(Niu et al. 2019)
N719	Pt	EL-HPE	735	19.2	0.70	9.84	2019	(Hora et al. 2019)
N719	CF@PANI@ CoSe	I^-/I_3^-	734	17.7	0.77	10.1	2019	(Zhang et al. 2019)
XW41+ Z1	Pt	I_2, LiI, PMII, tBP	726	19.6	0.72	10.2	2019	(Zeng, Lu, et al. 2019)
XW40+ Z1	Pt	I_2, LiI, PMII, tBP	748	19.6	0.72	10.6	2019	(Zeng, Lu, et al. 2019)
N719	(SPC-Co)	I_2, LiI, DPMII, tBP	730	21.4	0.68	10.6	2019	(Wu et al. 2019)
XW50	Pt	I_2, LiI, PMII, tBP	761	19.0	0.70	10.1	2019	(Zeng et al. 2019)
XW51	Pt	I_2, LiI, PMII, tBP	781	20.1	0.70	11.1	2019	(Zeng et al. 2019)
N719	Pt	I_2, BMII, tBP, GuSCN	790	21.6	0.65	11.1	2019	(Wan et al. 2019)
JY57+JY59	Pt	I_2, LiI, DPMII, tBP, GuSCN	787	18.2	0.67	9.56	2020	(Dai et al. 2020)
N719	Ni-MoSex @$CoSe_2$	I_2, LiI, DPMII, tBP	815	17.3	0.68	9.58	2020	(Liu et al. 2020)
D2 (w/CDCA)	Pt	I_2, LiI, DPMII, tBP	790	20.0	0.65	10.2	2020	(Duvva et al. 2020)
N719	Pt	I_2, LiI, DPMII, C_9H_7N	710	22.1	0.67	10.4	2020	(Gupta et al. 2020)
SGT-149	Pt	I_2, LiI, DPMII, tBP	713	19.3	0.71	9.8	2020	(Ji et al. 2020)
SGT-149 +SGT-021	Pt	I_2, LiI, DPMII, tBP	722	22.1	0.71	11.3	2020	(Ji et al. 2020)
XW62	Pt	I_2, LiI, PMII, tBP	762	20.7	0.74	11.6	2020	(Zeng et al. 2020)

Table 1. (Continued)

Dye	CE	Electrolyte	V_{OC} (mV)	J_{SC} (mA·cm^{-2})	η_{FF}	η_{PCE} (%)	Year	Ref.
XW61	Pt	I_2, LiI, PMII, tBP	775	21.4	0.75	12.4	2020	(Zeng et al. 2020)
N719	GBC	I^-/I_3^-	700	26.2	0.67	12.4	2020	(Oh et al. 2020)
CRD-IV	Pt	I^-/I_3^- (DHS-Et23)	752	16.4	0.73	9.02	2021	(Wan et al. 2021)
N719	Cu-MOF/PEDOT	I_2, LiI, $LiClO_4$	786	17.5	0.69	9.45	2021	(Yang et al. 2021)
N719	$NiCo_2S_4$ NRs/CNFs	I_2, LiI, TBAI, tBP	677	23.8	0.59	9.47	2021	(Qiu et al. 2021)
N719	Co_2P-NCNTs	I_2, LiI, DPMII, tBP	770	18.3	0.69	9.76	2021	(Chen et al. 2021)
N719	CuTGR	Iodolyte	745	19.9	0.66	9.81	2021	(Dhonde et al. 2021)
N719+ Coomassie R-250	Pt	I_2, LiI, BMIT, tBP	890	15.9	0.76	10.9	2021	(Kharkwal et al. 2021)
N719	$CoSe_2$/G-1	I^-/I_3^-	810	22.3	0.71	12.2	2021	(Tamilselvi et al. 2021)
BDTT-im-Cd	Pt	I_2, LiI, DPMII, tBP	790	15.6	0.74	9.13	2022	(Tian et al. 2022)
N719	Fe/Fe_3C @NHCF	I_2, LiI, DPMII, tBP	775	18.1	0.67	9.37	2022	(Wang et al. 2022)
Z907	Pt	I_2, LiI, TBAI, tBP	746	19.5	0.65	9.43	2022	(He et al. 2022)
RR14+ Y123	Pt	I_2, LiI, DMII, tBP, GuSCN	662	20.9	0.61	9.44	2022	(Watson et al. 2022)
N719	Co_9S_8-Ni_3S_2@WS_2	I_2, LiI, DPMII, tBP	833	17.7	0.66	9.67	2022	(Liu et al. 2022)
N719	BFTO/CN-50	I^-/I_3^-	751	22.9	0.67	11.2	2022	(Karthick et al. 2022)

Dye N719 is still regarded as the standard ruthenium sensitizer, as evidenced by Table 1. This sensitizer is almost exclusively employed when modifications are suggested on the photoanode such as:

- Doping the titania layer with Cu and N (Park et al. 2016; Dhonde et al. 2018) or Cu and S (Gupta et al. 2020) to increase the surface area and dye adsorption, delaying charge carrier recombination;
- Including TiO_2 nanorods, which boosts the charge transfer rate of the photogenerated electrons and also enhances the specific surface area (Wan et al. 2019);
- Adding nanocomposites of TiO_2 and graphene to improve the photocurrent and the resistance to charge recombination because it provides an effective pathway for electrons to flow within the external circuit (Mehmood et al. 2018; Dhonde et al. 2021).

N719 is also employed as a reference dye when testing new catalytic materials. A quasi core–shell structure of N-doped graphene/cobalt sulfide demonstrated high conductivity and catalytic activity due to close interactions between the cobalt sulfide core and the N-doped graphene shell. This resulted in high FF due to low resistance for the reduction of I_3^- to I^- on the counter-electrode surface, and increased V_{OC} through lower overpotential in the I_3^- reduction, favoring the regeneration step (Bi et al. 2014).

$CoSe_2$ (Jia et al. 2017) and Co–Cu–WS_x nanospheres (Qian et al. 2019) also demonstrated excellent capability to accelerate the reduction of I_3^-. Co-Fe-MoS_x (C. Xu et al. 2018), CoS nanosheets arrays (Feng et al. 2019), quaternary porous nanocubes Cu-Ni-$CoSe_x$ (Niu et al. 2019), porous carbon-cobalt composite (Wu et al. 2019), $CoSe_2$/graphene (Tamilselvi et al. 2021), Fe_3C with N-doped hollow carbon flower (Wang et al. 2022), Co_9S_8-Ni_3S_2@WS_2 (Liu et al. 2022), and $Bi_5FeTi_3O_{15}$@C_3N_4 (Karthick et al. 2022) showed more catalytically active sites, faster electron charge transfer, and higher electrocatalytic activity towards the reduction of I_3^-, decreasing the overpotential and, therefore, increasing the photovoltage.

Some of the drawbacks of ruthenium complexes are low molar extinction coefficients (between 10 000 and 20 000 M^{-1} cm^{-1}), limited absorption in longer wavelengths of the solar spectrum (near-IR), and scarcity of the noble metal, entailing an extra recycling fee (Błaszczyk 2021; Goncalves et al. 2008; Ito 2011). On the other hand, organic dyes are cheaper and more environmentally friendly as they are metal-free. The high molar extinction

coefficients (50 000 and 200 000 M^{-1} cm^{-1}) allow for thinner photoanodes, and the structural design of organic dyes is much more flexible (Błaszczyk 2021; Hagfeldt et al. 2010). Generally, organic dyes are designed based on the donor–π-bridge–acceptor architecture, or D–π–A (Figure 10). In this structure, the HOMO band is mainly attributed to the donor and the electron-rich π-bridge, whereas the LUMO is confined to the acceptor and anchoring groups. Hence, it is simple to tune the energy level of the HOMO/LUMO bands by changing the donor/π-bridge/acceptor groups (Zhang et al. 2013). The D–π–A architecture enables an intramolecular charge transfer complex, resulting in π-orbital overlap and subsequent red-shift in the absorption bands (Ji et al. 2020).

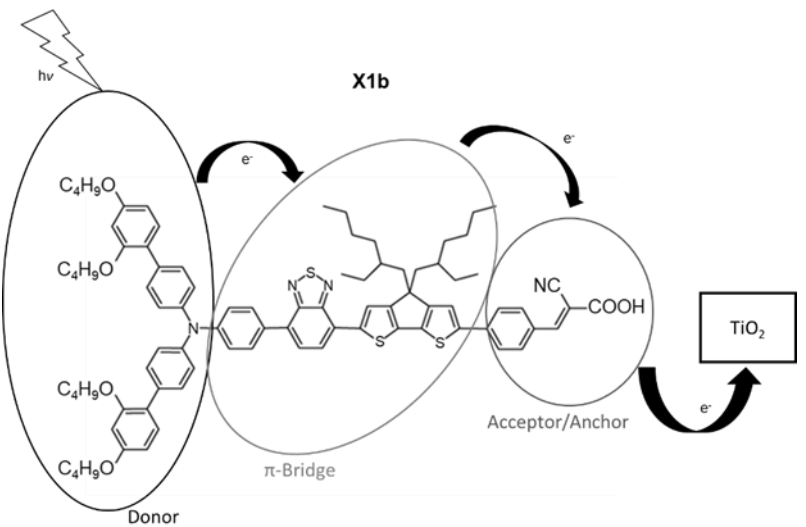

Figure 10. Schematic drawing of an organic dye with a D–π–A architecture, using the X1b dye to demonstrate the concept.

In addition to ruthenium sensitizers, organic sensitizers have also been successfully paired with iodine electrolytes. One of the first and most successful attempts was a D–π–A porphyrin sensitizer developed by Bessho et al. (Bessho et al. 2010). A diarylamino group was attached to the porphyrin ring as an electron donor, the porphyrin chromophore was used as π bridge, and an ethynylbenzoic acid moiety as an electron acceptor. A PCE of 11.0% was reported as a result of the increased light-harvesting properties of the photoanode due to the addition of a thin layer of larger reflecting particles (Bessho et al. 2010). Other works showed the versatility of this architecture

and achieved overall efficiencies above 10% (Krishna et al. 2017; Yang et al. 2017; Jiang et al. 2018; Han et al. 2018) (Table 1). Zeng et al. developed a new sensitizer with a doubled strapped porphyrin framework and a bulky 2,4-bis(hexyloxy)phenyl group incorporated into a phenothiazine donor, coded XW51. This dye contributed to a remarkable V_{OC} of 781 mV because the bulky donor had long alkoxyl chains as substituents, forming a compact self-assembled monolayer to hinder the penetration of the triiodide ion, to culminate in a PCE of 11.1% (Zeng et al. 2019) (Table 1).

Achieving panchromaticity when designing a new dye is a big task, thus many researchers have focused on the alternative method of co-sensitization. It is a challenging approach, but when employed correctly, it can enhance light absorption and broaden the spectral range by using two (or more) dyes with complementary absorption spectra. Nonetheless, this is a demanding strategy as the process of anchoring the co-sensitizers onto the semiconductor film is extremely competitive, which can hinder the adsorption of the dye cocktail (Lin et al. 2017).

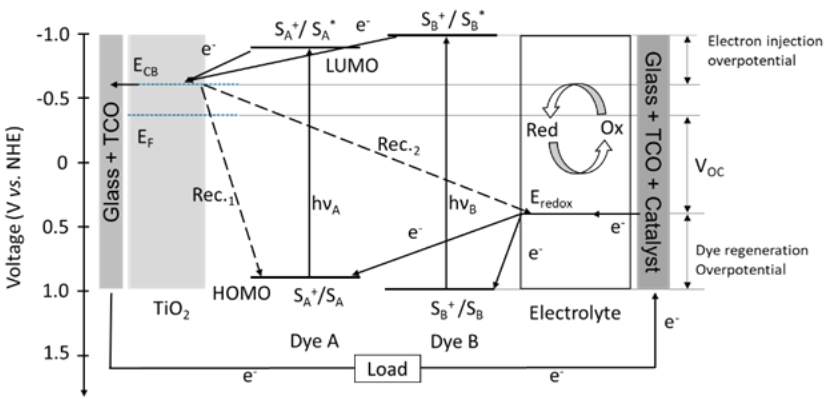

Figure 11. Schematic representation of the energy levels in a co-sensitized DSSC, between the semiconductor, dye A and B, electrolyte, and counter-electrode; forward reactions are represented by full arrows and recombination reactions are represented by dashed arrows (adapted from Cole et al. 2019).

The operating principle of a co-sensitized DSSC is similar to a conventional single-dye DSSC, as illustrated in Figure 11 (Cole et al. 2019); the main differences are slightly larger electron injection and dye regeneration overpotential. However, proper selection of complementary sensitizers could increase the LHE, leading to higher photocurrent, and minimizing the